Low Temperature Physics/Fizika Nizkikh Temperatur, 2015, v. 41, No. 10, pp. 1009–1023

Vortex dynamics in thin elliptic ferromagnetic nanodisks

G.M. Wysin

Department of Physics, Kansas State University, Manhattan, KS 66506-2601
E-mail: wysin@phys.ksu.edu

Received March 17, 2015, published online August 25, 2015

Vortex gyrotropic motion in thin ferromagnetic nanodisks of elliptical shape is described here for a pure vortex state and for a situation with thermal fluctuations. The system is analyzed using numerical simulations of the Landau–Lifshitz–Gilbert (LLG) equations, including the demagnetization field calculated with a Green's function approach for thin film problems. At finite temperature the thermalized dynamics is found using a second order Heun algorithm for a magnetic Langevin equation based on the LLG equations. The vortex state is stable only within a limited range of ellipticity, outside of which a quasi-single-domain becomes the prefered minimum energy state. A vortex is found to move in an elliptical potential, whose force constants along the principal axes are determined numerically. The eccentricity of vortex motion is directly related to the force constants. Elliptical vortex motion is produced spontaneously by thermal fluctuations. The vortex position and velocity distributions in thermal equilibrium are Boltzmann distributions. The results show that vortex motion in elliptical disks can be described by a Thiele equation.

PACS: **75.75.+a** Magnetic properties of nanostructures;
85.70.Ay Magnetic device characterization, design, and modeling;
75.10.Hk Classical spin models;
75.40.Mg Numerical simulation studies.

Keywords: magnetics, dipolar field, demagnetization, vortex dynamics, nanoparticles.

1. Introduction: Vortex dynamics in thin nanodisks

The magnetic vortex state in a thin nanodisk is an intriguing stable yet dynamic state [1,2], for appropriate disk radius a and thickness L. It attracts attention for application as an oscillator [3,4] and for data storage [5]. The vortex state has been mostly studied in nanodisks [6,7] with a circular perimeter due to the high symmetry, often made from Permalloy-79.

Thin film magnetic nanodots of elliptical shape have been studied for their magnetization reversal properties [8] and as elements for artificial spin ice arrays [9]. In this article the changes expected for vortex dynamics in a disk of elliptical perimemter are considered. Especially, it is important to consider how the deviation from perfect circular symmetry affects the time dynamics of a vortex. A second related goal is to determine the limits of stability of the vortex state when subjected to the non-circular boundary of an elliptical nanodisk.

A vortex state can be the ground state when centered in a circular disk, in contrast to either a quasi-single-domain state or some multi-domain state. A vortex is characterized by a curling of the nearly planar magnetization around a localized core region centered at point **R**, where the magnetization points perpendicular to the plane of the disk. This structure gives the vortex a topological charge or gyrovector **G** that interacts with applied forces and is essential in determining the dynamics [10,11]. If produced away from the disk center, a central force $F = -k_F R$, where k_F is a force constant, acts on the vortex [12]. This force is due to combined effects of exchange interactions and demagnetization effects that generate magnetic pole density on the disk edge. When interacting with the gyrovector, the force leads to a periodic orbital motion of the vortex core around the disk center known as gyrotropic motion [13,14], that can be excited by pulsed magnetic field [15]. The motion has been described in terms of the Thiele equation [10,11], which predicts the gyrotropic frequency as $\omega_G = k_F/G$. In circular disks, different predictions [12,16–18] for k_F result in ω_G roughly proportional to L/a [13,19].

For an elliptical disk, the breaking of the circular symmetry can be expected to modify the potential experienced by the vortex into one that has different force constants k_x and k_y along the two principal axes of the ellipse. Of course, for an ellipse of high enough eccentricity, the qua-

si-single-domain state will be prefered over a vortex state. The goal here is to study how the gyrotropic frequency is determined by the eccentricity, and as a part of that, to determine the changes in the force constants with ellipse shape. A byproduct is that the stability limit of the vortex state with ellipse shape will emerge.

A Lagrange-constrained micromagnetics simulation [12] is used here to determine quasi-static vortex force constants, as determined naturally from the microscopic exchange interactions and the demagnetization field energy. A constraint is used to hold a vortex with a desired core position **R**, from which calculation of the total microscopic energy gives a vortex effective potential $U(\mathbf{R})$. Knowledge of this effective potential is used in the Thiele equation for analysis of vortex core motion theoretically. The vortex motion also is studied by simulations of the microscopic time dynamics via micromagnetics [20,21] either for zero temperature, solved by fourth order Runge–Kutta (RK4) integration, or for finite temperature, using a Langevin equation for the magnetization dynamics, solved by a second order Heun algorithm. At finite temperature, the gyrotropic motion is spontaneously generated [22] just due to thermal fluctuations, further analyzed in earlier work [16]. The results of these studies provide support for using the Thiele equation in vortex analysis in non-circular disks. Further, effects are calculated as functions of ellipse shape and size, and some asymptotic rules are found for large disk size and moderate eccentricity.

The system energetics and calculational techniques are described in Sec. 2. Results for force constants from quasi-static vortex structures are found in Sec. 3. The modifications to Thiele dynamics, and gyrotropic frequencies for an elliptical disk are discussed in Sec. 4. Thermally generated vortex gyrotropic motion is considered in Sec. 5, and the main conclusions of these studies are summaried in Sec. 6.

2. Elliptic nanodisk magnetic system

The magnetic system is a thin elliptical disk of magnetic material such as Permalloy with saturation magnetization M_s, deposited on a nonmagnetic substrate. The disk has height L (along *z*-axis) perpendicular to the substrate. The perimeter of the disk in the *xy*-plane is assumed to be an ellipse with semi-major axis a and semi-minor axis *b*, defined by the equation

$$\frac{x^2}{a^2}+\frac{y^2}{b^2}=1. \tag{1}$$

The volume of magnetic material in the disk is $V = \pi abL$. Instead of the eccentricity $\sqrt{1-b^2/a^2}$ to characterize the shape, we find that the ellipticity or geometric aspect ratio is more relevant for this problem, defined by

$$\varepsilon = b/a \le 1. \tag{2}$$

The goals of this study include finding how the vortex gyrotropic frequency ω_G is affected by the elliptical shape of the nanodisk, as characterized by ellipticity. An important aspect of this study is to determine the effective potential $U(\mathbf{R})$ in which a vortex in the nanodisk moves. This requires a determination of the energy for placing a vortex with its core at different positions **R**. The energy as determined by the local magnetization **M**(**r**) will be used to describe the magnetization dynamics, and as well, to find the vortex effective potential $U(\mathbf{R})$.

2.1. Energetics

The microscopic energetics is assumed to be dominated by exchange energy and demagnetization energy (or equivalently, magnetostatic energy). The continuum Hamiltonian for the system is taken as

$$\mathcal{H} = \int dV \left\{ A\nabla\mathbf{m}\cdot\nabla\mathbf{m} - \frac{1}{2}\mu_0\mathbf{H}^M\cdot\mathbf{M} \right\}, \tag{3}$$

where A is the exchange stiffness (around 13 pJ/m for Permalloy), **M** is the spatially varying magnetization within the disk, and **m** is the magnetization scaled by the saturation value,

$$\mathbf{m} = \mathbf{M}/M_s\,. \tag{4}$$

In addition, the Hamiltonian includes the permeability of free space μ_0 on the interactions of the demagnetization field $\mathbf{H}^M$ that is itself generated by **M.** There is no external applied field considered here.

It is assumed that locally the magnetization stays saturated with $|\mathbf{M}(\mathbf{r})| = M_s$, however, its direction changes over a length scale $\lambda_{\rm ex}$ known as the exchange length. Equating the exchange energy term (of order $A/\lambda_{\rm ex}^2$) with the demagnetization energy term (of order $(1/2)\mu_0 M_s^2$, because also $\mathbf{H}_M$ is of order M_s) leads to the definition of the exchange length,

$$\lambda_{\rm ex} = \sqrt{\frac{2A}{\mu_0 M_s^2}}\,. \tag{5}$$

Exchange is dominant over lengths less than $\lambda_{\rm ex}$. Any significant variations in the direction of the magnetization take place over distances greater than $\lambda_{\rm ex}$.

While exchange interactions are considered local, the demagnetization field is determined by the global configuration of **M**. From Gauss' Law for magnetism, $\nabla\cdot\mathbf{B} = 0$, with magnetic induction $\mathbf{B} = \mu_0(\mathbf{H}^M + \mathbf{M})$, the demagnetization field satisfies

$$\nabla\cdot\mathbf{H}^M = -\nabla\cdot\mathbf{M}. \tag{6}$$

This is solved formally by introducing a scalar potential Φ_M such that $\mathbf{H}^M = -\nabla\Phi_M$, which then gives a Poisson equation for the magnetistatics problem,

$$-\nabla^2\Phi_M = \rho_M\,, \qquad \rho_M \equiv -\nabla\cdot\mathbf{M}. \tag{7}$$

Thus, the instanteous magnetization distribution determines the demagnetization field $\mathbf{H}^M$ via an effective magnetic charge density ρ_M.

2.2. Thin film demagnetization field

For a very thin magnet with $L \ll a$ and $L \ll b$, demagnetization energy leads to a natural tendency to keep **M** nearly within the plane of the film [23]. Further, there is little variation in **M** through the thickness of the film. For this situation, an effective two-dimensional (2D) Green's function approach can be used [24], leading to a 2D magnetostatics problem for $\mathbf{H}^M$. This is done by averaging all responses over the *z*-coordinate through the thickness of the magnetic film. This was implemented in our previous studies [16] on vortex dynamics in circular nanodisks, where effective 2D Green's functions give the demagnetization field components ($\alpha = x, y, z$) by convolutions,

$$H_\alpha^M(\mathbf{r}) = \int d^2\mathbf{r}' \sum_{\beta=x,y,z} G_{\alpha\beta}(\mathbf{r}-\mathbf{r}')M_\beta(\mathbf{r}'). \qquad (8)$$

The nonzero elements of the Green's function matrix are G_{xx}, G_{yy}, G_{zz} and $G_{xy} = G_{yx}$. The problem is separated: H_z^M perpendicular to the plane is determined solely by M_z while H_x^M and H_y^M are determined only by in-plane components M_x and M_y. Because the *z*-dependence has been averaged over, **r** and $\mathbf{r}'$ are 2D position vectors. Letting $\tilde{\mathbf{r}} = \mathbf{r} - \mathbf{r}'$ be a 2D displacement, the out-of-plane Green's function for $\tilde{\mathbf{r}} = |\tilde{\mathbf{r}}| > 0$ is

$$G_{zz}(\tilde{\mathbf{r}}) = \frac{1}{2\pi L}\left(\frac{1}{\sqrt{\tilde{r}^2 + L^2}} - \frac{1}{\tilde{r}}\right). \qquad (9)$$

Primarily, G_{zz} generates the field due to magnetic poles ($\sigma_M = \pm\hat{z}\cdot\mathbf{M}$) on the top and bottom surfaces of the magnetic film. The other components of $G_{\alpha\beta}$ generate the fields due to variations in **M** over the *xy* plane and also the magnetic pole charges on the perimeter of the ellipse (with thickness *L*). For $\tilde{r} > 0$, these components are

$$G_{xx}(\tilde{\mathbf{r}}) = \frac{L}{2\pi\tilde{r}^4}\left(\frac{\tilde{x}^2}{\sqrt{\tilde{r}^2 + L^2}} - \frac{\tilde{y}^2}{\sqrt{\tilde{r}^2 + L^2} + \tilde{r}}\right), \qquad (10)$$

$$G_{xy}(\tilde{\mathbf{r}}) = \frac{L}{2\pi\tilde{r}^4}\frac{2\sqrt{\tilde{r}^2 + L^2} + \tilde{r}}{\sqrt{\tilde{r}^2 + L^2} + \tilde{r}}\frac{\tilde{x}\tilde{y}}{\sqrt{\tilde{r}^2 + L^2}} \qquad (11)$$

with swapping $\tilde{x}$ and $\tilde{y}$ displacements to otain G_{yy} and G_{yx}. At large distances, these are the field of a point dipole in the *xy*-plane. Whether finding the vortex potential or evolving time dynamics, the field $\mathbf{H}^M$ has a strong influence on the energetics, and its calculation is the most time-consuming part of the numerics.

2.3. The 2D micromagnetics approach

We use a micromagnetics [20,21,25] calculation for the magnetization $\mathbf{M}(\mathbf{r}_i, t) \to M_s \hat{m}_i(t)$, where the 2D system is partitioned into cells i at positions $\mathbf{r}_i$. A single layer of cells of height L in the *z*-direction (perpendicular to the film) and square cross section $a_{\text{cell}} \times a_{\text{cell}}$ in the *xy*-plane are used. See Fig. 1 for a typical partitioning of a nanodisk with a vortex present into cells. The cells are set symmetrically within the ellipse, Eq. (1). In some cell labeled i there is a time-dependent unit magnetization $\hat{m}_i(t)$, such that the magnetic moment is $\boldsymbol{\mu}_i = La_{\text{cell}}^2 M_s \hat{m}_i$. Then, discretization of the continuum Hamiltonian (3) leads to the 2D micromagnetics Hamiltonian in a form [16]

$$\mathcal{H} = -J\left[\sum_{(i,j)} \hat{m}_i \cdot \hat{m}_j + \frac{a_{\text{cell}}^2}{2\lambda_{\text{ex}}^2}\sum_i \tilde{H}_i^M \cdot \hat{m}_i\right], \qquad (12)$$

where i, j label micromagnetics cells, and the exchange constant between nearest-neighbor cells is

$$J = 2AL. \qquad (13)$$

The demagnetization field enters scaled by the saturation magnetization of the medium,

$$\tilde{H}_i^M = \mathbf{H}_i^M / M_s. \qquad (14)$$

The factor involving exchange length indicates how exchange effects become more dominant for large exchange length. For the assumptions of the micromagnetics approach to be valid, one should have adequately small cell size, $a_{\text{cell}} < \lambda_{\text{ex}}$, making the demagnetization term a perturbation on the exchange term.

The Green's matrix $G_{\alpha\beta}$ also must be discretized on the lattice of cells. The contribution to the $\mathbf{H}^M$ field at position **r** from a source cell at $\mathbf{r}_i$ is proportional to $G_{\alpha\beta}(\mathbf{r} - \mathbf{r}_i)a_{\text{cell}}^2$, including the area a_{cell}^2 of the source cell. The elements of $G_{\alpha\beta}$ become singular at $\tilde{r} \to 0$, as for any Green's operator for a self-interaction. That derivation, however, did not account correctly for $\tilde{r} = 0$ because it was assumed that the field was measured outside the source cell. A given cell can also produce a finite averaged demagnetization field within itself, however, so the point $\tilde{r} = 0$ needs to be treated correctly. We do this [12,16] by using the Green's function components averaged over a circle whose area is equivalent to the cell area a_{cell}^2. The components of $G_{\alpha\beta}$ at the origin $\tilde{r} = 0$ are replaced by their values averaged over the circle of radius r_0, such that $\pi r_0^2 = a_{\text{cell}}^2$. This gives

$$G_{zz}(0) = \langle G_{zz}\rangle_0 = -\frac{1}{La_{\text{cell}}^2}\left(L + r_0 - \sqrt{L^2 + r_0^2}\right). \qquad (15)$$

This is the same as $G_{zz}(0) = -N_z / a_{\text{cell}}^2$, where N_z is the longitudinal demagnetization factor of a cylinder that gives the internal field due to surface magnetic charges at its ends. The factor of cell area a_{cell}^2 cancels out when the

integral (8) is converted to a sum. In a similar way, averaging the transverse components of $G_{\alpha\beta}$ over a circle of radius r_0 leads to setting $G_{xy}(0) = G_{yx}(0) = 0$ and

$$G_{xx}(0) = G_{yy}(0) = \langle G_{xx}\rangle_0 = -\frac{1}{2La_{\rm cell}^2}\left(\sqrt{L^2+r_0^2} - r_0\right). \quad (16)$$

This is the same as $G_{xx}(0) = -N_x/a_{\rm cell}^2$ and $G_{yy}(0) = -N_y/a_{\rm cell}^2$, where $N_x = N_y$ is the transverse demagnetization factor for a cylinder. For long thin circular cylinders, the formula gives the expected value $N_x = N_y \approx 1/2$. One can see that the requirement $N_x + N_y + N_z = 1$ is then reflected in the relation

$$G_{xx}(0) + G_{yy}(0) + G_{zz}(0) = \frac{1}{a_{\rm cell}^2}. \quad (17)$$

With the Green's matrix defined on a square grid, the calculation of $\mathbf{H}^M$ can be accelerated by the use of a fast Fourier transform (FFT) approach [26], replacing the convolution integral in real space with a product in reciprocal space. Thus, we choose a $N\times M$ grid with a binary size $2^n \times 2^m$, where n and m are integers such that $2(2a) \le Na_{\rm cell}$ and $2(2b) \le Ma_{\rm cell}$. This ensures that the computation grid is at least twice the size of the ellipse along both axes. That is necessary to avoid the wrap-around problem of the FFT, so that the simulation gives the demagnetization field of an isolated nanodisk, without interaction effects due to aliasing. The FFT of $G_{\alpha\beta}$ can be done once at the start of the calculations, but then FFT's of the magnetization configuration are continuually carried out at every step of the simulations. The (x, y) coordinate system is then set up with the origin at the center of the ellipse, and the x-axis along the semi-major axis (a), and the y-axis along the semi-minor axis (b).

2.4. Dynamics

Each cell has a magnetic moment $\boldsymbol{\mu}_i = \mu\hat{m}_i$, where the magnitude is $\mu = La_{\rm cell}^2 M_s$. With the definition of the Hamiltonian (12), each cell's dynamics is governed by a Landau–Lifshitz–Gilbert torque equation [27,28], including a dimensionless damping parameter α,

$$\frac{d\boldsymbol{\mu}_i}{dt} = \gamma\boldsymbol{\mu}_i\times\mathbf{B}_i - \frac{\alpha}{\mu}\boldsymbol{\mu}_i\times\left(\gamma\boldsymbol{\mu}_i\times\mathbf{B}_i\right). \quad (18)$$

γ is the gyromagnetic ratio and $\mathbf{B}_i$ is the effective magnetic field acting on the cell, obtained from

$$\mathbf{B}_i = -\frac{\delta\mathcal{H}}{\delta\boldsymbol{\mu}_i}. \quad (19)$$

It is convenient to define a unit of magnetic induction B_0 and dimensionless field $\mathbf{b}_i = \mathbf{B}_i/B_0$ and corresponding dimensionless time τ by

$$B_0 = \frac{J}{\mu} = \frac{2AL}{La_{\rm cell}^2 M_s} = \frac{\lambda_{\rm ex}^2}{a_{\rm cell}^2}\mu_0 M_s, \qquad \tau = \gamma B_0 t. \quad (20)$$

Then the dynamics follows an equation in dimensionless quantities,

$$\frac{d\hat{m}_i}{d\tau} = \hat{m}_i\times\mathbf{b}_i - \alpha\hat{m}_i\times(\hat{m}_i\times\mathbf{b}_i), \quad (21)$$

where the dimensionless field is

$$\mathbf{b}_i = \frac{\mathbf{B}_i}{B_0} = \sum_{j\in z(i)}\hat{m}_j + \frac{a_{\rm cell}^2}{\lambda_{\rm ex}^2}\frac{\tilde{H}_i^M}{2}. \quad (22)$$

The first term involves a sum only over the nearest neighbors $z(i)$ of site i; the second term shows how the demagnetization field effect depends on the cell size. These fields are used to determine the quasi-static vortex properties, such as force constants in the vortex effective potential. The LLG equation in the form (21) is also used here to get gyrotropic frequencies for pure vortex states at zero temperature, solving it by a fourth order Runge–Kutta integrator.

For time dynamics at nonzero temperature, thermal fluctuations can be included by changing to a corresponding Langevin equation based on the Landau–Lifshitz-Gilbert equation [16], by including a damping term with parameter α and stochastic magnetic inductions $\mathbf{b}_s$ caused by temperature. Suppressing the cell index i for simplicity, the Langevin-LLG equation for one cell is

$$\frac{d\hat{m}}{d\tau} = \hat{m}\times(\mathbf{b}+\mathbf{b}_s) - \alpha\hat{m}\times[\hat{m}\times(\mathbf{b}+\mathbf{b}_s)]. \quad (23)$$

The net dynamics is a combination of the deterministic motion due to $\mathbf{b}$ modified by the stochastic effects due to $\mathbf{b}_s$. The strength of these stochastic fields is determined through the fluctuation-dissipation theorem, which can be stated as

$$\langle b_s^{\lambda}(\tau) b_s^{\lambda'}(\tau')\rangle = 2\alpha\mathcal{T}\delta_{\lambda\lambda'}\delta(\tau-\tau'). \quad (24)$$

Indices $\lambda\lambda'$ refer to Cartesian components, which appear in a Kronecker delta function on the RHS. The Dirac delta function $\delta(\tau-\tau')$ shows the instantenous time correlation of the fields. Their amplitudes are ultimately related to the strength of damping and the dimensionless temperature $\mathcal{T}$, defined as

$$\mathcal{T} \equiv \frac{k_B T}{J} = \frac{k_B T}{2AL} \quad (25)$$

where k_B is Boltzmann's constant. The stochastic fields must be generated to satisfy (24). For numerical solution of these Langevin-LLG equations, that is accomplished by solving them with a second order Heun method [29,30], see further details in Ref. 16. Essentially, the second order Heun method is the same as a predictor-corrector method

where the predictor stage is an Euler step and the corrector stage is the trapezoid rule. The same random fields $\mathbf{b}_s$ used in the predictor step, generated by a random number generator, are re-used in the corrector step. The fluctuation-dissipation theorem (24) is implemented by choosing random fields with a variance σ_s that depends on the time step $\Delta\tau$, according to

$$\sigma_s = \sqrt{2\alpha T \Delta\tau}. \tag{26}$$

That is, in the equations integrated over one time step, an individual stochastic field component b_s^x is effectively replaced by a random number of variance σ_s by doing

$$\int_{\tau}^{\tau+\Delta\tau} d\tau\, b_s^x(\tau) \to \sigma_s r, \tag{27}$$

where r is a uniformly random number of zero mean and unit variance. The usual uniform deviate from 0 to 1 from a random number generator has a variance of $1/\sqrt{12}$. We used the generator [31] *mzran*13 to produce uniform deviates from 0 to 1, shifted them to the range –0.5 to +0.5, and finally rescaled by $\sqrt{12}\,\sigma_s$ to get stochastic fields of the correct distribution.

Simulations were done by supposing that Permalloy is the medium, with values A = 13 pJ/m, M_s = 860 kA/m, which results in exchange length $\lambda_{ex} \approx 5.3$ nm. For most simulations we used cell size parameter $a_{\text{cell}} = 2.0$ nm. Then with gyromagnetic ratio $\gamma \approx 1.76 \cdot 10^{11}$ T^{-1} s^{-1}, one has field strengths $\mu_0 M_s = 1.08$ T and $B_0 = 7.59$ T. The time unit is then $t_0 \equiv (\gamma B_0)^{-1} \approx 0.750$ ps, which also implies a frequency unit $f_0 = t_0^{-1} = 1.336$ THz.

3. Relaxed vortex structure calculations

Determination of the vortex potential $U(\mathbf{R})$ requires a precise static solution of the Hamiltonian (3) or equivalently, one with zero time derivatives as determined from the zero-temperature limit of (23), putting all $\mathbf{b}_s = 0$. A pure isolated vortex structure is also important for initiation of dynamics simulations. Here an approach for generating a pure vortex structure, such as those in Fig. 1, without the presence of spin waves, is summarized.

The magnetization can be described by an in-plane angle $\varphi(\mathbf{r})$ and out-of-plane angle $\theta(\mathbf{r})$,

$$\hat{m}(\mathbf{r}) = (\cos\theta(\mathbf{r})\cos\varphi(\mathbf{r}), \cos\theta(\mathbf{r})\sin\varphi(\mathbf{r}), \sin\theta(\mathbf{r})). \tag{28}$$

For a vortex state whose core is centered at $\mathbf{R} = (X, Y)$, the in-plane angle is approximately

$$\varphi(\mathbf{r}) = q\tan^{-1}\frac{y-Y}{x-X} \tag{29}$$

where $q = +1$ is the vorticity. For the numerical studies here, we start with this in-plane structure and let the out-of-plane structure develop naturally by a relaxation procedure with a constraint on the desired vortex core position [12]. In this "spin alignment" relaxation procedure, each cell's

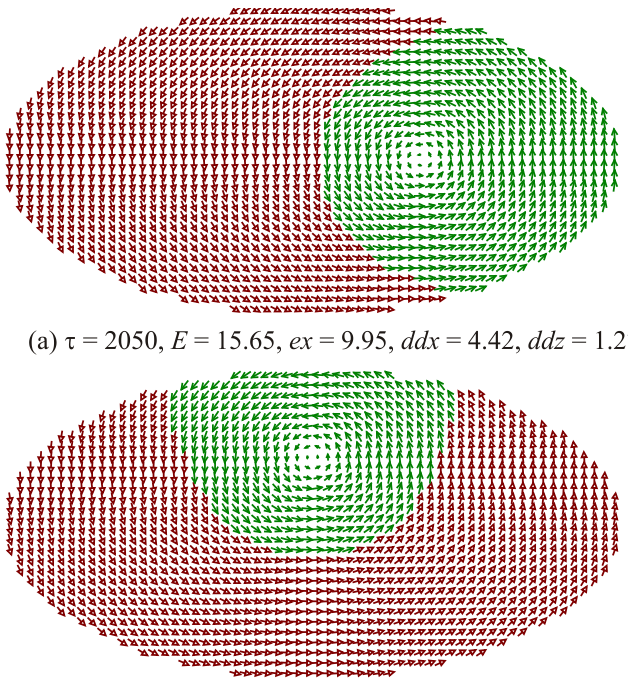

(a) τ = 2050, E = 15.65, ex = 9.95, ddx = 4.42, ddz = 1.27

(b) τ = 3250, E = 15.65, ex = 9.33, ddx = 4.99, ddz = 1.33

Fig. 1. (Color online) Vortex structures at times (a) τ = 2050 and (b) τ = 3250, for a disk with a = 60 nm, ε = 0.5, and L = 10 nm. The cell size is a_{cell} = 2 nm. Arrows show only the projection of (m_i^x, m_i^y) on the page. Green line (red open) arrows indicate positive (negative) values of m_i^z. The core appears as a hole in this projection. Exchange, in-plane and out-of-plane demagnetization energies are *ex*, *ddx*, and *ddz*, respectively. The vortex was initiated at (0,16 nm) from the disk center with Lagrange-constrained relaxation. It has been evolved forward in time via RK4 with damping α = 0.02 turned off at τ = 1600. The gyrotropic motion is clockwise.

$\hat{m}_i$ is iteratively redirected [32] to the direction of its effective field $\mathbf{b}_i$, until the changes are insignificant. Once all $\hat{m}_i$ are aligned with the corresponding $\mathbf{b}_i$, the time derivatives will be zero and the configuration will be static. However, to enforce a desired position, fictitious extra fields are added to $\mathbf{b}_i$ in the core region by a Lagrange undetermined multipliers technique. The details of the Lagrange relaxation procedure are given in Ref. 12. The undetermined fields become determined in the procedure, which requires a similar constraint for unit length of each $\hat{m}_i$. The fictitious fields in the core region produce torques that secure the vortex without changing its internal structure significantly. While this relaxation proceeds, the out-of-plane structure in $\theta(r)$ develops, if one initiates the configuration with some small random z-components in the magnetization field.

3.1. Vortex gyrotropic motion

At the vortex core, the relaxed configuration has $m_z(X, Y) \approx \pm 1$, and m_z diminishes with radius away from the core. The two signs are energetically equivalent polari-

zations $p = \pm 1$ of the core, and due to the slight randomness in initial conditions, either one may result. The vortex dynamics is then strongly influenced by the product of qp, which enters into the so-called gyrovector (a type of topological charge),

$$\mathbf{G} = G\hat{z} = 2\pi pq\frac{m_0}{\gamma}\hat{z}. \tag{30}$$

The factor $2\pi pq = \pm 2\pi$ is the solid angle of the unit sphere covered by the magnetization profile, and $m_0 = \mu/a_{\rm cell}^2 = LM_s$ is the magnetic moment per unit area in the film. The gyrovector is known to be important for vortex dynamics, because it enters in the Thiele equation for describing the motion of the core, according to

$$\mathbf{F} + \mathbf{G}\times\mathbf{V} = 0, \qquad \mathbf{V} = \dot{\mathbf{R}}, \tag{31}$$

where the dot on $\mathbf{R}$ indicates time derivative, such that $\mathbf{V}$ is the cortex core velocity. The force $\mathbf{F}$ is the negative gradient of the total vortex energy with respect to vortex core position, i.e.,

$$\mathbf{F} = -\nabla U(\mathbf{R}). \tag{32}$$

Here any damping or intrinsic vortex mass is not included. Primarily, we are concerned with the determination of $U(\mathbf{R})$ for the elliptic system and analyzing whether the vortex motion can be described by a Thiele equation. This can be fairly generally expected, however, the Thiele equation dynamics is expected whenever the vortex structure is nearly fixed in shape while it translates to different positions.

In the case of a circular nanodisk, the force on a vortex is essentially a restoring force that points towards the disk center, with a force constant k_F :

$$\mathbf{F} = -k_F\,\mathbf{R}. \tag{33}$$

This then corresponds to a circularly symmetric parabolic potential (near the center of the disk),

$$U(\mathbf{R}) = \frac{1}{2}k_F\mathbf{R}^2 = \frac{1}{2}k_F(X^2+Y^2). \tag{34}$$

The force constant has been estimated by various methods, including the rigid vortex approximation [18], the two-vortex model [17,18], and numerical simulations [12,16]. Regardless of the method, this potential then predicts a uniform circular motion of the vortex core, at instantaneous velocity

$$\mathbf{V} = \frac{\mathbf{G}\times\mathbf{F}}{G^2} = \boldsymbol{\omega}_G\times\mathbf{R}. \tag{35}$$

The rotational angular frequency is

$$\boldsymbol{\omega}_G = -\frac{k_F}{G}\hat{z}\,. \tag{36}$$

Thus, a vortex with positive gyrovector ($pq = +1$, $\mathbf{G}$ pointing along $+\hat{z}$) will rotate in the clockwise sense in the xy-plane, and one with negative gyrovector ($pq = -1$) rotates in the counterclokwise sense. It is important to see how this uniform circular motion is modified for elliptical nanodisks.

3.2. Vortex potential in elliptical disks

For an elliptical nanodisk with perimeter from (1), relaxed vortex structures were generated by the spin alignment algorithm [12], using a Lagrange constraint to enforce different vortex core locations $\mathbf{R} = (X,Y)$. $\mathbf{R}$ near the origin (the center of the disk) is of most interest. The results of those studies for different aspect ratios ε and semi-major axes a indicate that the vortex effective potential is close to quadratic near the disk center, and can be approximated by

$$U(\mathbf{R}) = U_0 + \frac{1}{2}(k_X X^2 + k_Y Y^2). \tag{37}$$

The constant U_0 is the total energy for the vortex centered in the disk. Due to the distortion of the disk compared to a circular disk, there are nonequal force constants k_x and k_y for the two semi-major axis directions. We restrict the studies to situations with $a \geq b$ or $\varepsilon \leq 1$; the long axis of the ellipse is along the x-axis. Then, there is a lower energy cost for displacement of the vortex in the long direction of the ellipse, and $k_x \leq k_y$. The force constants were estimated by fitting to (37), after finding the total system energy for a centrally located vortex, $\mathbf{R} = 0$, and for small displacements $\mathbf{R} = (2a_{\rm cell}, 0)$ and $\mathbf{R} = (0, 2a_{\rm cell})$, where $a_{\rm cell} = 2.0$ nm was the cell size. Calculations were done for two different film thicknesses, $L = 5.0$ nm and $L = 10$ nm. Generally, the force constants increase approximately as L^2, similar to the L-dependence for circular nanodisks.

The energies of relaxed vortex configurations were calculated in units of $J = 2AL$, and with displacements in units of cell size $a_{\rm cell}$, in earlier work [16] values of k_F for circular disks were initially calculated in units of $A/a_{\rm cell}$. That unit depends on cell size. Instead, results for force constants are quoted here in a more natural unit of $A/\lambda_{\rm ex} = \frac{1}{2}\mu_0 M_s^2\lambda_{\rm ex}$, which combines both the exchange and demagnetization energy scales.

Force constant results for $L = 5.0$ nm and various a, as functions of the ellipticity or aspect ratio $\varepsilon = b/a$, are shown in Fig. 2. Further results at twice the thickness, $L = 10.0$ nm, are displayed in Fig. 3. The shapes of the curves are very similar to those for $L = 5.0$ nm, however, the force constants are larger, approximately in proportion to L^2. At the circular limit $\varepsilon = 1$, one has $k_x = k_y$ and these values decrease with increasing nanoparticle radius, approximately as a^{-1}. As ε becomes less than **1**, the longitudinal force constant k_x decreases while the transverse force constant k_y increases. However, once ε reaches

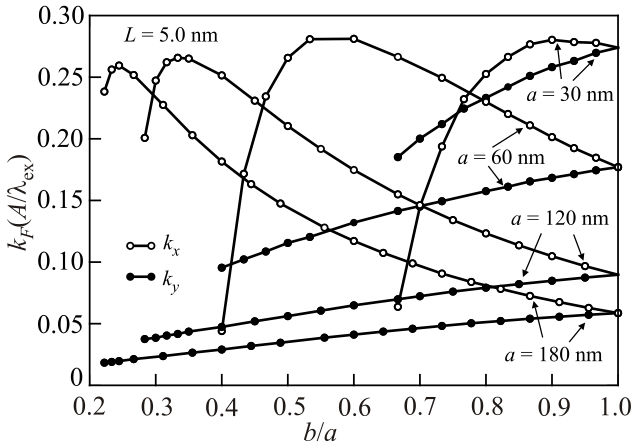

Fig. 2. Vortex force constants along the semi-major axis (k_x, solid circles) and along the semi-minor axis (k_y, open circles) for different sized ellipses with thickness L = 5.0 nm, organized by semi-major axis a, plotted versus ellipticity ratio $\varepsilon = b/a$.

some lower limit, depending on a, the vortex state becomes unstable, as would be the case even for circular disks of very small size. Obviously, the limit as $\varepsilon \to 0$ will lead to a needle-like nanodisk, whose ground state will be a quasi-single-domain state, once the aspect ratio is high enough. In the region where the vortex state is destabilized, k_y reaches either a maximum value, or even turns over and in the case of smaller disks (especially $a = 30$ nm), it is possible for k_y to become less than k_x.

The fact that k_y is greater than k_x is understandable in terms of the energetics of magnetic pole density generated on the perimeter of the ellipse. When the vortex is displaced along the semi-major axis (x axis), extra pole density $\sigma_M = \hat{n}\cdot\mathbf{M}$ primarily appears along the long edges at $y \approx \pm b$. The pole strength is weak, because $\mathbf{M}$ will be able to align parallel to these long edges. In the opposite case of vortex displacement along the semi-minor axis (y axis), the

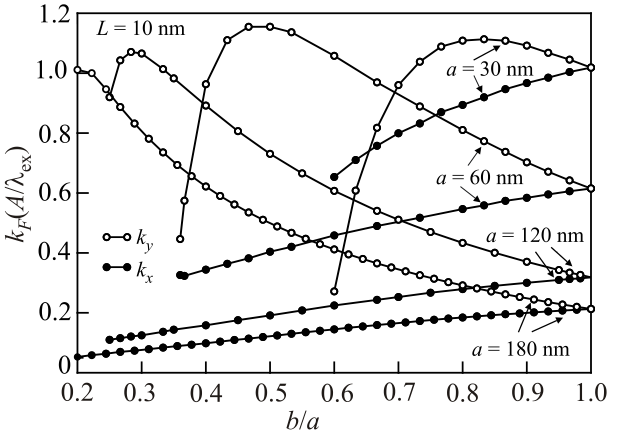

Fig. 3. Vortex force constants versus ellipticity ratio $\varepsilon = b/a$ as in Fig. 1, but for film thickness L = 10.0 nm. Note that larger thickness leads to higher force constants, roughly proportional to L^2.

pole density will appear primarily at the pointed ends at $x \approx \pm a$. Because there is a larger curvature there, it is more difficult for $\mathbf{M}$ to remain parallel to the perimeter at these ends, leading to a larger pole density. Also, the greater proximity of the vortex to the edges at $y \approx \pm b$ leads to greater energy effects for a displacement in the y direction. In either case, the energy should be proportional to the demagnetization field integrated over nanodisk volume, however, the weaker poles for displacement of the vortex along the long axis makes k_x less than k_y. In the plots, one sees that k_x appears to extrapolate towards a value of zero as $\varepsilon \to 0$, consistent with these arguments.

The dependence of k_x and k_y on ellipticity can be further analyzed by first looking at how these force constants influence the vortex gyrotropic motion. This is done initially from the theoretical view of applying the Thiele equation to the vortex dynamics.

4. Thiele equation dynamics for elliptic nanodisks

Here it is assumed that the vortex motion obeys the Thiele equation, using the potential (37) as determined from k_x and k_y. The orbital frequency, trajectory, and other basic properties are of most interest.

First, it is interesting to note that the motion is not the same as for a 2D harmonic oscillator with nonequal force constants, because the x and y motions are not independent. With gyrovector $\mathbf{G} = G\hat{z}$, the components of the Thiele equation (31), using the force from potential (37) give

$$F_x = -k_x X = -(\mathbf{G}\times\mathbf{V})_x = G\dot{Y}\,,$$
$$F_y = -k_y Y = -(\mathbf{G}\times\mathbf{V})_y = -G\dot{X}\,. \qquad (38)$$

The components can be easily separated, and each follows the same second order differential equation, namely,

$$\ddot{X} = -\frac{k_x k_y}{G^2}X, \qquad \ddot{Y} = -\frac{k_x k_y}{G^2}Y. \qquad (39)$$

One can see that the geometric mean of the force constants will determine the gyrotropic frequency. However, it is best to maintain the coupling of comoponents and express the first order equations in matrix form,

$$\frac{d}{dt}\begin{pmatrix} X \\ Y \end{pmatrix} = \begin{pmatrix} 0 & k_y/G \\ -k_x/G & 0 \end{pmatrix}\begin{pmatrix} X \\ Y \end{pmatrix}. \qquad (40)$$

Then letting the 2×2 matrix on the RHS be called A, the solution is written formally as

$$\begin{pmatrix} X(t) \\ Y(t) \end{pmatrix} = \mathrm{e}^{At}\begin{pmatrix} X_0 \\ Y_0 \end{pmatrix} \qquad (41)$$

where the initial position is $\mathbf{R}(0) = (X_0, Y_0)$. Expansion of the exponential is simple because the square of A is

$$A^2 = -\frac{k_x k_y}{G^2} I, \tag{42}$$

where I is the 2×2 identity matrix. At this point one can define the gyrotropic frequency,

$$\omega_G = -\frac{\sqrt{k_x k_y}}{G}. \tag{43}$$

The negative square root has been used, such that a vortex with G in the positive $\hat{z}$ direction has a negative frequency, corresponding to its clockwise movement in the *xy*-plane. Then the time development proceeds from

$$e^{At} = I\cos\omega_G t + \frac{A}{\omega_G}\sin\omega_G t. \tag{44}$$

Thus, the vortex motion is found to be elliptical,

$$X(t) = X_0\cos\omega_G t + Y_0\frac{k_y}{G\omega_G}\sin\omega_G t\,,$$

$$Y(t) = Y_0\cos\omega_G t - X_0\frac{k_x}{G\omega_G}\sin\omega_G t\,. \tag{45}$$

Differentiation gives the vortex core velocity,

$$\dot{X}(t) = -\omega_G X_0\sin\omega_G t + \frac{k_y Y_0}{G}\cos\omega_G t\,,$$

$$\dot{Y}(t) = -\omega_G Y_0\sin\omega_G t - \frac{k_x X_0}{G}\sin\omega_G t\,. \tag{46}$$

One can then verify that the motion follows the equation (35) just as for circular nanodisks, namely,

$$V_x = \frac{1}{G^2}(\mathbf{G}\times\mathbf{F})_x = \frac{k_y}{G}Y,$$

$$V_y = \frac{1}{G^2}(\mathbf{G}\times\mathbf{F})_y = -\frac{k_x}{G}X. \tag{47}$$

4.1. Transforming to circular coordinates

The last results might be expected, especially since the elliptical system can be thought of as a distortion of a circular system by rescaling the axes. Conversely, consider the distortion of the elliptical system back to an equivalent circular system.

The potential can be symmetrized with respect to semi-major and semi-minor axes in the sense that

$$U(\mathbf{R}) = \frac{1}{2}[(\sqrt{k_x}X)^2 + (\sqrt{k_y}Y)^2] =$$

$$= \frac{1}{2}\sqrt{k_x k_y}\left(\sqrt{\frac{k_x}{k_y}}X^2 + \sqrt{\frac{k_y}{k_x}}Y^2\right). \tag{48}$$

This suggests the definition of the energetic ellipticity *e*,

$$e \equiv \sqrt{\frac{k_x}{k_y}}, \tag{49}$$

as well as the geometric average of the force constants,

$$\bar{k} \equiv \sqrt{k_x k_y}. \tag{50}$$

Then the potential is

$$U(\mathbf{R}) = \frac{1}{2}\bar{k}\left(eX^2 + \frac{1}{e}Y^2\right). \tag{51}$$

One can see that e also relates to the ellipticity of the vortex core motion, from the solution obtained above, for example, with $Y_0 = 0$,

$$\frac{Y_{\max}}{X_{\max}} = \frac{k_x}{G|\omega_G|} = \sqrt{\frac{k_x}{k_y}} = e. \tag{52}$$

The solution for vortex core position can be expressed in a similar symmetrized way, first scaling X by $\sqrt{k_x}$ and Y by $\sqrt{k_y}$:

$$\sqrt{k_x}X(t) = \sqrt{k_x}X_0\cos\omega_G t - \sqrt{k_y}Y_0\sin\omega_G t\,,$$

$$\sqrt{k_y}Y(t) = \sqrt{k_y}Y_0\cos\omega_G t + \sqrt{k_x}X_0\sin\omega_G t\,. \tag{53}$$

Note that the change in sign on the second terms (compared to Eq. (45)) is due to using equation (43) for gyrotropic frequency. However, the potential in the form (51) can be expressed in a circular coordinate $\boldsymbol{\rho}$ defined as follows,

$$U(\boldsymbol{\rho}) = \frac{1}{2}\bar{k}\boldsymbol{\rho}^2, \qquad \boldsymbol{\rho} \equiv \left(\sqrt{e}X, \frac{1}{\sqrt{e}}Y\right). \tag{54}$$

Thus, this shows the scaling needed on X and *Y*. Then the solution (45) can be expressed in these circular coordinates as a uniform circular motion, e.g.,

$$\sqrt{e}X(t) = \sqrt{e}X_0\cos\omega_G t - \frac{1}{\sqrt{e}}Y_0\sin\omega_G t\,,$$

$$\frac{1}{\sqrt{e}}Y(t) = \frac{1}{\sqrt{e}}Y_0\cos\omega_G t + \sqrt{e}X_0\sin\omega_G t. \tag{55}$$

With initial position $\boldsymbol{\rho}_0 = (\rho_{x0}, \rho_{y0}) = (\sqrt{e}X_0, Y_0/\sqrt{e})$, this is

$$\rho_x(t) = \rho_{x0}\cos\omega_G t - \rho_{y0}\sin\omega_G t = \rho\cos(\varphi_0 + \omega_G t)\,,$$

$$\rho_y(t) = \rho_{y0}\cos\omega_G t + \rho_{x0}\sin\omega_G t = \rho\sin(\varphi_0 + \omega_G t)\,. \quad (56)$$

The radius is conserved at $\rho = \sqrt{\rho_{x0}^2 + \rho_{y0}^2}$, while φ_0 is the initial angle to the *x*-axis,

$$\tan\varphi_0 = \frac{\rho_{y0}}{\rho_{x0}} = \frac{1}{e}\frac{Y_0}{X_0}. \quad (57)$$

Then the time-dependent angle to the *x*-axis simply increases linearly in time,

$$\varphi(t) = \varphi_0 + \omega_G t. \quad (58)$$

Note that the angular position of the vortex core in the original coordinates, $\theta = \tan^{-1}(Y/X)$, is related to φ also by the energetic ellipticity,

$$\tan\theta(t) = \frac{Y}{X} = \frac{\sqrt{e}\rho_y}{\frac{1}{\sqrt{e}}\rho_x} = e\tan\varphi(t). \quad (59)$$

For the core velocity $\mathbf{V} = (\dot{X}, \dot{Y})$, one finds for the gyrotropic motion

$$\mathbf{V} = \omega_G\left(-\frac{1}{e}Y, eX\right) = \omega_G\left(-\frac{1}{\sqrt{e}}\rho_y, \sqrt{e}\rho_x\right). \quad (60)$$

The corresponding expression for the time derivative of $\boldsymbol{\rho}$ carries a greater simplicity,

$$\dot{\rho}_x = \sqrt{e}\dot{X} = -\omega_G\rho_y\,, \qquad \dot{\rho}_y = \frac{1}{\sqrt{e}}\dot{Y} = \omega_G\rho_x \quad (61)$$

which is equivalent to the expected expression for uniform circular motion,

$$\dot{\boldsymbol{\rho}} = (\dot{\rho}_x, \dot{\rho}_y) = \boldsymbol{\omega}_G \times \boldsymbol{\rho}. \quad (62)$$

This is based on the assumption that the vector angular velocity is $\boldsymbol{\omega}_G = \omega_G\hat{z}$. Therefore the motion is equivalent to that for circular nanodisks, once transformed into these circular coordinates.

4.2. Further analysis of force constants

In light of the above results expected from the Thiele equation dynamics, it makes sense to further analyze the force constants found from the vortex relaxation algorithm. In particular, we now see that $\bar{k} = \sqrt{k_x k_y}$ directly determines the gyrotropic frequency, while $e = \sqrt{k_x/k_y}$ determines the shape of the path followed by the vortex core.

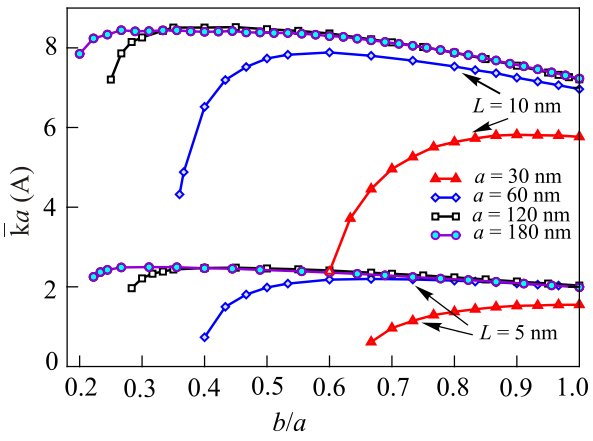

Fig. 4. (Color online) The geometric mean of force constants, $\bar{k} = \sqrt{k_x k_y}$, scaled by semi-major axis *a*, in units of the exchange stiffness *A*, versus geometric ellipticity $\varepsilon = b/a$.

Based on the force constant results for L = 5.0 nm and L = 10.0 nm, $\bar{k}$ has been calculated and the results plotted versus aspect ratio ε are shown in Fig. 4. $\bar{k}$ is found to scale with the reciprocal of the semi-major axis, hence, the results for $\bar{k}a$ versus ε are displayed. Especially for large a, there appears to be an asymptotic limit in the functional dependence, $\bar{k}(\varepsilon)$. For the smaller ellipses ($a \le 60$ nm), the scaling of $\bar{k}$ as $1/a$ is not present. In addition to this dependence on the size of the xy perimeter, it is also observed that $\bar{k}$ increases almost as fast as L^2. Of course, the vortex gyrotropic frequency ω_G should be directly proportional to $\bar{k}$, hence Fig. 3 should also give a sense of the dependence of ω_G on the nanodisk shape. But note that the magnitude of the gyrovector depends on film thickness,

$$G = 2\pi pqLM_s/\gamma. \quad (63)$$

The dependence of G on film thickness cannot be ignored when considering gyrotropic frequencies.

Next, the calculated values of energetic ellipticity $e = \sqrt{k_x/k_y}$ are shown in Fig. 5 for L = 5.0 nm and in Fig. 6 for L = 10.0 nm, as functions of ε. The results for different semi-major axis sizes tend to fall close to the same linear relation,

$$e = \varepsilon, \quad \text{or} \quad \sqrt{\frac{k_x}{k_y}} = \frac{b}{a}, \quad (64)$$

which is shown as a dashed line. The matching to this approximate fit is best for the largest elliptical particles, and especially when ε approaches unity. Thus, there is some simplicity in the force constants, provided the system is far from the stability limit of the vortex state. This requires, however, reasonably large sized nanondisks and/or a strong quasi-2D aspect with both $L \ll a$ and $L \ll b$.

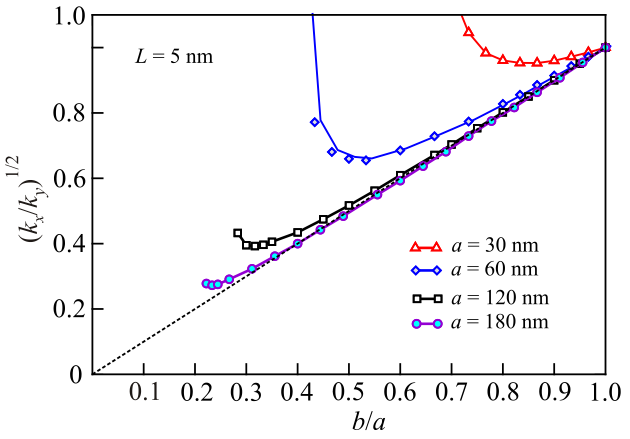

Fig. 5. (Color online) The energetic ellipticity for L = = 5.0 nm, as calculated from the square root of the ratio of forces constants, $e = \sqrt{k_x/k_y}$, versus geometric ellipticity $\varepsilon = b/a$.

4.3. Gyrotropic frequencies from simulations

For some selected shapes of elliptic nanoparticles, the gyrotropic vortex motion was simulated based on the magnetization dynamics, as it evolves according to the zero temperature LLG equations (21). For these studies the time evolution was found using RK4 with time step $\Delta\tau = 0.04$, starting from an initial state with vortex core at desired position by the Lagrange constrained relaxation method. An initial 4.0 nm displacement from the disk center was used. An example of vortex structure and motion with a large initial dispacement for showing structural details is shown in Fig. 0. The damping constant $\alpha = 0.02$ was used for further relaxing the structure over close to one period of the motion, and then set to zero. The period t_G was determined from five or more subsequent revolutions, from which estimates of the gyrotropic frequencies $f_G = 1/t_G$ or $\omega_G = 2\pi f_G$ were made. These could be analyzed in light of the force constants $\bar{k}$ calculated on the same system, assuming the motion follows the Thiele equation dynamics.

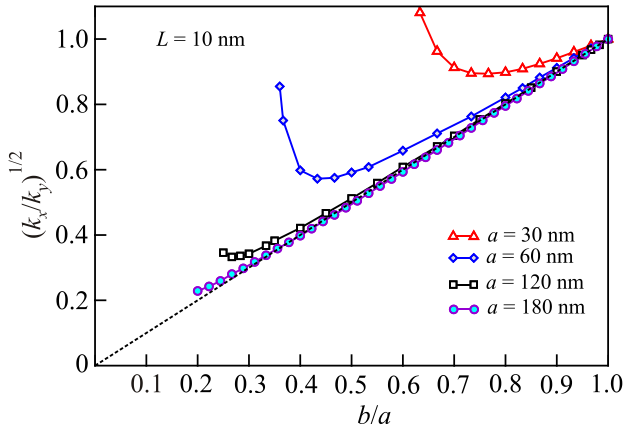

Fig. 6. (Color online) The energetic ellipticity for L = 10 nm, as defined from the square root of the ratio of forces constants, $e = \sqrt{k_x/k_y}$, versus geometric ellipticity $\varepsilon = b/a$.

The vortex period could be determined either from observing oscillations of the components of total system magnetization, or from the trajectory of the vortex core.

For analysis of the trajectory followed by the vortex core, an algorithm is needed to locate the core position $(X(t), Y(t))$ precisely. The core is the point with maximum magnitude of out-of-plane magnetization around which the magnetization has a nonzero rotation. This was done by first locating the computation cell containing the vorticity center, where $|\nabla\times\nabla\varphi| = 2\pi$ is a nonzero rotation of $\hat{m}$ around the cell. Then, neighboring cells out to a distance of $r\lambda_{ex}$ were used to further refine the position estimate by weighting their position contributions with $(m_i^z)^2$, giving a better estimate of the location where m^z is maximimum. It is found that this procedure is adept at locating the core even in the presence of thermal fluctuations [16]. It is applied for that purpose in the next section.

From the expression (62) for G and the definition of the exchange length, the gyrotropic frequency magnitude can be expressed in a form using λ_{ex} as the physical length scale, and A/λ_{ex} as the unit for force constants,

$$|\omega_G| = \frac{\bar{k}}{G} = \left(\frac{\mu_0}{4\pi}\gamma M_s\right)\left(\bar{k}\,\frac{\lambda_{ex}}{A}\right)\left(\frac{\lambda_{ex}}{L}\right). \qquad (65)$$

This displays a natural SI unit of angular frequency, $\omega_0 \equiv (\mu_0\gamma M_s)/4\pi$ (the same as γM_s in CGS units). Results for the frequencies in these units, found from simulations, are shown in Fig. 6, as functions of the ellipticity parameter $\varepsilon = b/a$. The curves for $\omega_G(\varepsilon)$ show an increase with decreasing ε as ε deviates away from unity, similar to the curves of $\bar{k}(\varepsilon)$. When the vortex state begins to reach its limit of stability, $\omega_G(\varepsilon)$ makes a much faster drop with decreasing ε.

To check whether expression (64) applies to these results, and to show the dependence of ω_G on film thickness, the frequencies divided by dimensionless force constants are plotted in Fig. 8, again versus ε. Data at different semimajor axes a = 30 nm, 60 nm and 120 nm are found to collapse onto the straight dotted lines corresponding to expression (64) for the selected values of thickness L. This shows that the calculations of force constants can be used to predict gyrotropic frequencies, in conjunction with use of the Thiele theory even for elliptic disks.

5. Thermal equilibrium statistics

In this section the spatial distribution of a vortex in a nanodot in thermal equilibrium is considered. The analysis is based on supposing that the dynamics is following the Thiele equation, but with thermal fluctuations. To proceed, it is important to verify the canonical coordinates for the motion of the vortex core. Based on that, the Boltzmann distribution can be applied to the vortex statistics.

5.1. Vortex Lagrangian dynamics

Generalizing the Lagrangian for a vortex in a circular nanodisk [16] to the case of the elliptical potential $U(\mathbf{R})$, it is possible to show that an appropriate Lagrangian for the core motion is [16]

$$L = -\frac{1}{2}G(X\dot{Y} - Y\dot{X}) - \frac{1}{2}(k_x X^2 + k_y Y^2). \qquad (66)$$

Gyrotropic motion is similar to that of a charge q moving in a magnetic field, where the effective vector potential $\mathbf{A} = (\mathbf{G}\times\mathbf{R})/2 = (-GY, GX)/2$ generates the gyrovector by $\mathbf{G} = \nabla\times\mathbf{A}$. Then, the first term in L is $-\mathbf{A}\cdot\mathbf{V}$, just as a term $-q\mathbf{A}\cdot\mathbf{V}$ appears in the Lagrangian for a nonrelativistic charge. Then the Lagrangian is

$$L = -\mathbf{A}\cdot\mathbf{V} - U, \qquad (67)$$

when the anisotropic potential (37) is included. Its Euler-Lagrange equations correctly give the dynamics equations (38) found in Sec. 4.

In this symmetric choice of gauge, the momentum conjugate to core position $\mathbf{R}$ is

$$\mathbf{P} = \frac{\partial L}{\partial \mathbf{V}} = -\mathbf{A} = \frac{1}{2}(GY, -GX). \qquad (68)$$

Then the Lagrangian can be written as $L = \mathbf{P}\cdot\mathbf{V} - U$. However, the Hamiltonian is desired for statistical mechanics. It is obtained by the transformation

$$H = \mathbf{P}\cdot\mathbf{V} - L = U = \frac{1}{2}(k_x X^2 + k_y Y^2). \qquad (69)$$

This shows that the Thiele equation dynamics is derived purely from the potential. Note that alternatively the Landau gauge can be used [33] with a nonsymmetric momentum of one component, $P_x = GY$, which leads to the identical Hamiltonian, independent of the choice of gauge.

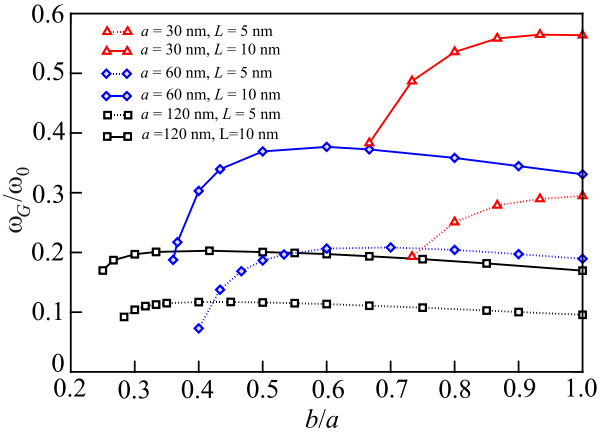

Fig. 7. (Color online) Vortex gyrotropic angular frequencies calculated from simulations of zero-temperature dynamics, for the indicated nanodisk sizes. The frequency unit is $\omega_0 \equiv (\mu_0\gamma M_s)/4\pi$ (about 15.1 GHz for Permalloy).

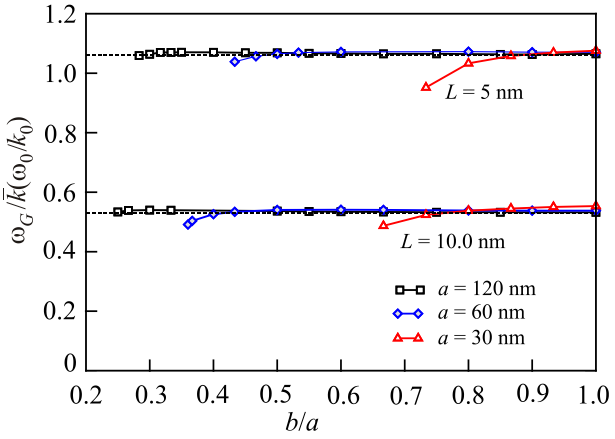

Fig. 8. (Color online) Vortex gyrotropic angular frequencies from zero-temperature simulations divided by force constants $\bar{k}$ from Lagrange constrained vortex relaxation, as a function of ellipticity $\varepsilon = b/a$. The frequency unit is $\omega_0 \equiv$ of ellipticity $\varepsilon =$ $= b/a$. The frequency unit is $\omega_0 \equiv (\mu_0\gamma M_s)/4\pi$, the force constant unit is $k_0 \equiv a/\lambda_{ex}$. Dashed lines are the theoretical result (64) based on the Thiele equation dynamics, where $\omega_G/\bar{k} \propto \lambda_{ex}/L$.

As Hamiltonian (69) has no momentum present, as written, it does not lead to correct dynamic equations of motion, based on the usual Hamilton equations of motion,

$$\dot{\mathbf{P}} = -\frac{\partial H}{\partial \mathbf{R}}, \qquad \dot{\mathrm{X}} = \frac{\partial H}{\partial \mathbf{P}}. \qquad (70)$$

This is because the connection (68) between momentum and coordinate makes them dependent. To get a Hamiltonian whose dynamics leads back to the Thiele equations, it is necessary to rewrite H not as purely a potential term, but as half potential energy involving $\mathbf{R}$ and half kinetic energy involving $\mathbf{P}$. Then H must be written

$$H = \frac{1}{4}(k_x X^2 + k_y Y^2) + \frac{1}{4}\left(\frac{2}{G}\right)^2 (k_x P_y^2 + k_y P_x^2), \qquad (71)$$

which does lead back to the correct Thiele equation. Although this resembles the Hamiltonian of a 2D harmonic oscillator, it bears repetition that the constraint $\mathbf{P} = -\mathbf{A} = -(\mathbf{G}\times\mathbf{R})/2$, between coordinate and momentum means that the vortex phase space is collapsed to only two dimensions, rather than four. Therefore, for the purposes of statistical equilibrium calculations, the mean thermal energy in vortex motions will be only $k_B T$, because there are only two independent quadratic variables in H, each receiving on average $(k_B T)/2$ of energy.

5.2. Vortex core radial distribution

In thermal equilibrium, the distribution for vortex core position or velocity should be determined by a Boltzmann factor, $\exp(-\beta H)$, where $\beta = (k_B T)^{-1}$ is the inverse reduced temperature and k_B is Boltzmann's constant. The vortex core Hamiltonian H can be expressed either purely

as potential energy, Eq. (69) or in terms of equal parts potential energy and kinetic energy, Eq. (71), or even in a third form with only a kinetic energy term. This is a somewhat unusual freedom and allows one to find either the distribution in real space or in velocity space.

In the effective circular coordinates $\boldsymbol{\rho}$ defined in (54) then the Hamiltonian expressed purely with potential energy is very simple and circularly symmetric,

$$H = U(\boldsymbol{\rho}) = \frac{1}{2}\bar{k}\rho^2. \tag{72}$$

The probability for the vortex core to be found in some range $d\rho$ near the radius ρ is proportional to

$$p(\rho)d\rho \sim 2\pi\rho\, d\rho\, e^{-\beta H} = 2\pi\rho\, d\rho\, e^{-\frac{1}{2}\beta\bar{k}\rho^2}. \tag{73}$$

Making this a unit normalized probability distribution, the result is

$$p(\rho) = \beta\bar{k}\rho\, e^{-\frac{1}{2}\beta\bar{k}\rho^2}. \tag{74}$$

This circularly symmetric form is best for comparison with simulations, because we have the value of $e = \sqrt{k_x/k_y}$ available that is necessary to get results into the circular coordinates. From equipartition one can arrive at the root-mean-square radius,

$$\langle H\rangle = k_BT \quad\Rightarrow\quad \rho_{\rm rms} = \sqrt{\frac{2}{\beta\bar{k}}}. \tag{75}$$

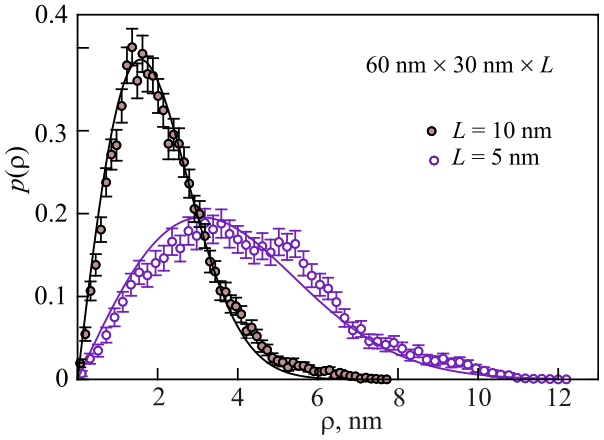

Fig. 9. (Color online) Vortex core position radial distributions at T = 300 K for semi-major axis a = 60 nm, ε = 0.5 for two disk thicknesses. Symbols are from Langevin LLG simulations out to dimensionless time $\tau = 2.5\cdot10^5$. Solid curves are the theoretical expression (73) with $\bar{k} = 4.299\cdot10^{-4}$ N/m for L = 5.0 nm and $\bar{k} = 1.676\cdot10^{-3}$ N/m for L = 10 nm, from relaxed vortex calculations. The T = 0 gyrotropic periods were $\tau_G \approx 2970$ for L = 5.0 nm and $\tau_G \approx 1500$ for L = 10 nm.

In addition, the mean radius and the most probable radius (where $p(\rho)$ is maximum) are

$$\langle\rho\rangle = \sqrt{\frac{\pi}{2\beta\bar{k}}}, \qquad \rho_{\rm max} = \sqrt{\frac{1}{\beta\bar{k}}}. \tag{76}$$

Simulations of the Langevin LLG equations were carried out to calculate some typical thermalized dynamics for a vortex in thermal equilibrium. The initial state is taken as a relaxed vortex at the center of a nanodisk. Using damping parameter α = 0.02, the integration was carried out to final dimensionless time $\tau = 2.5\cdot10^5$ by the second order Heun algorithm [29,30] with time step $\Delta\tau$ = 0.01. Depending on the gyrotropic periods this is a fairly large number of vortex revolutions. Even starting from the potential energy minimum, thermal fluctuations can initiate the gyrotropic motion spontaneously [22]. The result is a noisy gyrotropic orbital motion; examples in circular nanodisks were given in Ref. [16].

Distributions of the vortex core position away from the nanodisk center are shown in Fig. 9 for a = 60 nm and in Fig. 10 for a = 120 nm, both with ε = 0.5. The data are compared with the theoretical expression (74), applying the appropriate values of $\bar{k}$ from the Lagrange-relaxed vortex calculations. There is a good agreement here between theory and simulations, being better for larger L and smaller a. Of course, at larger L the gyrotropic period t_G is shorter, and averaging out to a fixed time is then done over more revolutions, leading to smaller errors. In addition, the system with larger a also has longer periods, hence its errors are greater, and averaging to a longer time would give a better fit to theory. The deviation between theory and simulation in Fig. 9 for L = 10 nm is typical for these simulations over a limited number of vortex periods, where on occasion for many periods, the vortex may move with noticably larger or smaller radius than normal from the disk center. This can be seen in Fig. 11, where both $X(\tau)$ and $\rho(\tau)$ are shown for the case of a = 120 nm, ε = 0.5, L = 10 nm.

The distribution in the original coordinates (X,Y) will certainly be elliptic, with the same ellipticity parameter e. The normalized probability distribution in (X,Y) is found as

$$p(X,Y) = \sqrt{\frac{\beta k_x}{2\pi}}e^{-\frac{1}{2}\beta k_xX^2}\sqrt{\frac{\beta k_y}{2\pi}}e^{-\frac{1}{2}\beta k_yY^2} \tag{77}$$

that is, a Gaussian in each coordinate, with variances inversely proportional to the corresponding force constants,

$$\sigma_x = \frac{1}{\sqrt{\beta k_x}}, \qquad \sigma_y = \frac{1}{\sqrt{\beta k_y}}. \tag{78}$$

Of course, the distributions in X separately from Y have zero mean, which makes them less useful than the distribution for ρ, with its peak at a finite value of ρ.

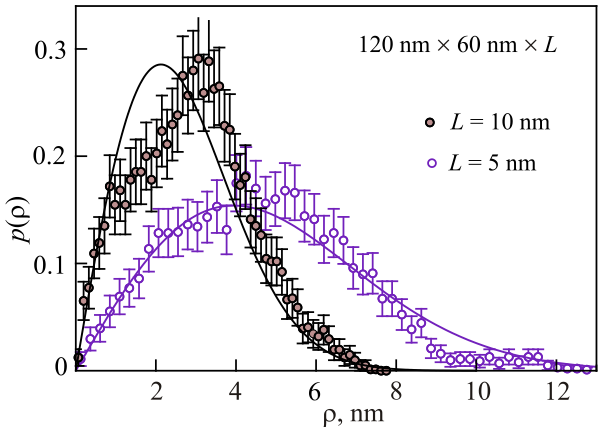

Fig. 10. (Color online) Vortex core position radial distributions at T = 300 K for semi-major axis a = 120 nm, ε = 0.5 for two disk thicknesses. Symbols are from Langevin LLG simulations out to dimensionless time $\tau = 2.5\cdot10^5$. Solid curves are the theoretical expression (73) with $\bar{k} = 2.667\cdot10^{-4}$ N/m for L = 5.0 nm and $\bar{k} = 9.174\cdot10^{-4}$ N/m for L = 10 nm, from relaxed vortex calculations. The T = 0 gyrotropic periods were $\tau_G \approx 4770$ for L = 5.0 nm and $\tau_G \approx 2760$ for L = 10 nm. The ρ(τ) used to produce the curve for L = 10 nm is displayed in Fig. 11.

An example of the vortex core distribution along the semi-major axes of a nanodisk are shown in Fig. 12 for a = = 120 nm, ε = 0.5 and thickness L = 10 nm. The simulation data are compared to the theoretical expression (76) by using the appropriate k_x and k_y force constants from Lagrange-relaxed vortex simulations. The greater value of k_y relative to k_x then leads to the expected narrower distribution in Y compared to X.

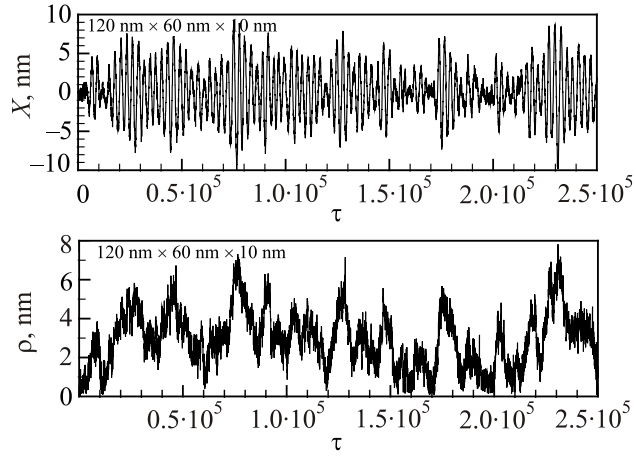

Fig. 11. Vortex core motion for thermalized dynamics at T = = 300 K for semi-major axis a = 120 nm, ε = 0.5, thickness L = = 10 nm. Graphs of $X(\tau)$ and $Y(\tau)$ are very similar, but of different amplitudes. The resulting equivalent circular radius ρ(τ) was used to produce the corresponding probability $p(\rho)$in Fig. 10.

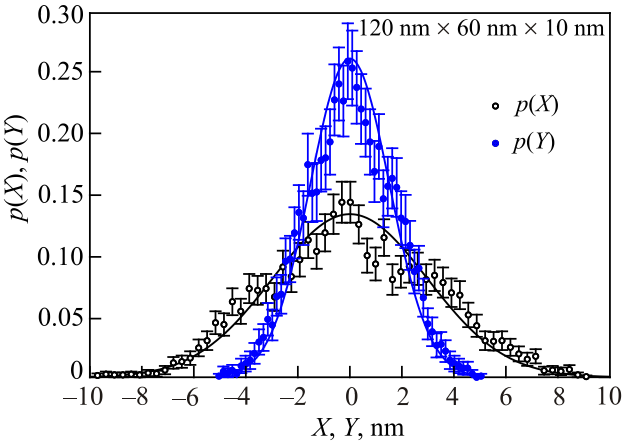

Fig. 12. Vortex core linear distributions along the major axes at T = 300 K for semi-major axis a = 120 nm, ε = 0.5, thickness L = 10 nm. Symbols are from Langevin LLG simulations to time $\tau = 2.5\cdot10^5$. Solid curves are from theoretical expression (77) with $k_x = 4.696\cdot10^{-4}$ N/m and $k_y = 1.792\cdot10^{-3}$ N/m, from relaxed vortex calculations.

5.3. Vortex core speed distribution

The result for $p(\rho)$ can also be mapped into a distribution for velocity, using the circular coordinate $\boldsymbol{\rho}$ and its velocity $\dot{\boldsymbol{\rho}}$. With velocity magnitude denoted u, then

$$u = |\dot{\boldsymbol{\rho}}| = |\omega_G|\rho. \tag{79}$$

Therefore, the distribution $g(u)$ in speed u is easily obtained by a rescaling of the distribution $p(\rho)$ in radius. Applying conserved probabilities,

$$p(\rho)d\rho = g(u)du = g(u)|\omega_G|d\rho, \tag{80}$$

then the normalized speed distribution can be obtained from

$$g(u) = |\omega_G|^{-1}\, p(u/|\omega_G|). \tag{81}$$

This results in

$$g(u) = \frac{\beta\bar{k}}{\omega_G^2} u e^{-\frac{1}{2}\beta\bar{k}u^2/\omega_G^2}. \tag{82}$$

However, using relations (43) and (50) for the frequency, this is expressed more directly from the force constants and the gyrovector,

$$g(u) = \frac{\beta G^2}{\bar{k}} u e^{-\frac{1}{2}\beta G^2 u^2/\bar{k}}. \tag{83}$$

Alternatively, the speed distribution is

$$g(u) = \frac{2u}{u_{rms}^2} e^{-u^2/u_{rms}^2}. \tag{84}$$

The rms speed used in the second form has been defined from the rms radius, e.g.,

$$u_{\rm rms} = |\,\omega_G\,|\,\rho_{\rm rms} = \sqrt{\frac{2\bar{k}}{\beta G^2}}. \tag{85}$$

This speed distribution might be compared with one for particles with kinetic energy $(m_G u^2)/2$, where m_G is an effective mass for gyrotropic motion. Then comparing the exponent in the first expression for $g(u)$ leads to a result,

$$m_G = \frac{G^2}{\bar{k}}. \tag{86}$$

G increases linearly with thickness L, while $\bar{k}$ is roughly proportional to L^2, so this mass is nearly independent of the film thickness. m_G depends on the nanodisk size primarily through the dependence of $\bar{k}$ on the nanoparticle area πab. However, the expected value for typical nanodisks will be extremely small (on the order of 10^{-23}–10^{-22} kg). This mass represents the inertia of the vortex in response to the applied forces, as mediated by the effects caused by the gyrovector. Certainly it is unusual in that it depends inversely on the force constant.

6. Conclusions

A combination of Lagrange-constrained vortex relaxation and time development of the LLG equations have been used to study single vortex dynamics in elliptically shaped magnetic nanodisks. The results have been analyzed in view of using the Thiele equation for the motion of the vortex core, where the core position **R** acts as a collective coordinate. Even the vortex relaxation results are interpreted by using **R** as the coordinate for the vortex effective potential $U(\mathbf{R})$. The vortex potential is approximately parabolic along the two principal axis directions, but only for displacements not approaching the edge of the nanodisk. A vortex moving very close to an edge will be strongly perturbed by its image vortex outside the system, an effect [34] not considered here that softens the potential in that region.

The force constants k_x and k_y in $U(\mathbf{R})$ have been determined for some different disk sizes and ellipticities $\varepsilon = b/a$, using the Lagrange-constrained spin-alignment relaxation procedure, holding the vortex in different positions to estimate the potential. Three interesting results emerge here: (1) There is a lower limit of ε below which the vortex solution is unstable towards the prefered formation of a quasi-single-domain state. For increasing semi-major axis a, this lower limit on ε becomes lower. (2) Starting from the circular limit, $\varepsilon = 1$, and moving towards lower values, k_x diminishes and is roughly proportional to ε, while k_y increases and is roughly dependent on ε^{-1}, see Figs.2 and 3. These are not precises statements, however, they hold more closely for larger semi-major axis a and over a wider range of ε. (3) As a result, the asymptotic dependence of the energetic ellipticity $e = \sqrt{k_x/k_y}$ on ε for large a is linear, $e \approx \varepsilon$, see Figs. 5 and 6. This then shows that vortex orbits at large a will have the same shape as the perimeter of the ellipse. These asymptotic results hold only weakly for smaller elliptical nanodisks, and only in the region ε closer to 1.

Concerning vortex dynamics in elliptical nanodisks, micromagnetic simulations have been used to determine the time evolution of the whole disk's magnetizaton, starting from a Lagrange-relaxed initial vortex. The vortex motion seen in micromagnetics simulation has been compared with the core motion expected from the Thiele equation. These results agree well, using the force constants k_x, k_y, from the static relaxed vortex calculations to make the comparison. The vortex gyrotropic frequency is predicted to be $\omega_G = -\bar{k}/G$, where $\bar{k} = \sqrt{k_x k_y}$ is the geometric mean of force constants. At zero temperature, this is confirmed in the micromagnetics, see Fig. 8. The gyrotropic frequencies ω_G obtained from micromagnetics, Figure 7, have a rather weak dependence on ε until the vortex stability limit is reached. The frequencies do increase approximately linearly with film thickness L, and for larger a, we also find $\omega_G \propto a^{-1}$, again only away from the stability limit. The behavior of $\bar{k}$ with ε and a, L, Fig. 3, can be used to predict gyrotropic frequencies, when included with the gyrovector $G \propto L$.

An effective circular coordinate ρ has been introduced, in which the vortex gyrotropic motion becomes uniform circular motion. This coordinate is more convenient for determination of the vortex core position distribution in thermal equilibrium. Longer simulations of the Langevin-LLG equations were used to get statistics for the vortex position over many orbits in equilibrium. Provided a large enough number of revolutions has been observed, one finds that indeed the distribution of vortex core position can be described with a Boltzmann distribution. Again, to make the proper comparison, the force constants k_x, k_y are needed. The force constant $\bar{k}$ determines the radial distribution $p(\rho)$; larger $\bar{k}$ naturally implies a smaller width. The force constants k_x and k_y determine the distributions of core position along the principal axes of the nanodisk, and again, the distribution widths decrease with increasing force constants. Thus, the determination of the effective vortex potential and its force constants is seen to be the most important element needed for understanding the dynamics in a noncircular magnetic nanodisk.

1. N.A. Usov and S.E. Peschany, *J. Magn. Magn. Mater*. **118**, 290 (1993).
2. J. Raabe, R. Pulwey, S. Sattler, T. Schweinbock, J. Zweck, and D. Weiss, *J. Appl. Phys*. **88**, 4437 (2000).
3. S. Kasai, Y. Nakatani, K. Kobayashi, H. Kohno, and T. Ono, *Phys. Rev. Lett*. **97**, 107204 (2006).

4. V.S. Pribiag, I.N. Krivorotov, G.D. Fuchs, P.M. Braganca, O. Ozatay, J.C. Sankey, D.C. Ralph, and R.A. Buhrman, *Nature Phys*. **3**, 498 (2007).
5. K.Yu. Guslienko, K.-S. Lee, and S.-K. Kim, *Phys. Rev. Lett*. **100**, 027203 (2008).
6. R.P. Cowburn, D.K. Koltsov, A.O. Adeyeye, M.E. Welland, and D.M. Tricker, *Phys. Rev. Lett*. **83**, 1042 (1999).
7. M. Schneider, H. Hoffmann, and J. Zweck, *Appl. Phys. Lett*. **77**, 2909 (2000).
8. Zung-Hang Wei, Mei-Feng Lai, Ching-Ray Chang, N.A. Usov, J.C. Wu, and Jun-Yang Lai, *J. Magn. Magn. Mater*. **272**, e563 (2004).
9. G.M. Wysin, W.A. Moura-Melo, L.A.S. Mól, and A.R. Periera, *J. Phys.: Condens. Matter* **24**, 296001 (2012).
10. A.A. Thiele, *Phys. Rev. Lett*. **30**, 230 (1973); *J. Appl. Phys*. **45**, 377 (1974).
11. D.L. Huber, *Phys. Lett*. **76A**, 406 (1980); *Phys. Rev. B* **26**, 3758 (1982).
12. G.M. Wysin, *J. Phys.: Condens. Matter* **22**, 376002 (2010).
13. K.Yu. Guslienko, B.A. Ivanov, V. Novosad, Y. Otani, H. Shima, and K. Fukamichi, *J. Appl. Phys*. **91**, 8037 (2002).
14. K.Yu. Guslienko, X.F. Han, D.J. Keavney, R. Divan, and S.D. Bader, *Phys. Rev. Lett*. **96**, 067205 (2006).
15. J.P. Park, P. Eames, D.M. Engebretson, J. Berezovsky, and P.A. Crowell, *Phys. Rev. B* **67**, 020403 (2003).
16. G.M. Wysin and W. Figueiredo, *Phys. Rev. B* **86**, 104421 (2012).
17. K.L. Metlov and K.Yu. Guslienko, *J. Magn. Magn. Mater*. **242**, 1015 (2002).
18. K.Yu. Guslienko, V. Novosad, Y. Otani, and K. Fukamichi, *Appl. Phys. Lett*. **78**, 3848 (2001).
19. B.A. Ivanov and C.E. Zaspel, *Appl. Phys. Lett*. **95**, 7444 (2004).
20. C.J. García-Cervera, *Magnetic Domains and Magnetic Domain Walls*, Ph.D. thesis, New York University, New York (1999).
21. C.J. García-Cervera, Z. Gimbutas, and E. Weinan, *J. Comp. Phys. E* **184**, 37 (2003).
22. T.S. Machado, T.G. Rappoport and L.C. Sampaio, *Appl. Phys. Lett*. **100**, 112404 (2012).
23. G. Gioia and R.D. James, *Proc. R. Soc. London Ser. A* **453** 213 (1997).
24. Zhongyi Huang, *J. Comp. Math*. **21**, No. 1, 33 (2003).
25. D. Suessa, J. Fidler, and T. Schrefl, *Handbook Magn. Mater*. **16**, 41 (2006).
26. J. Sasaki and F. Matsubara, *J. Phys. Soc. Jpn* **66**, 2138 (1997).
27. L.D. Landau and E.M. Lifshitz, *Phys. Z. Sowjet* **8**, 153 (1935).
28. F.H. de Leeuw, R. van den Poel, and U. Enz, *Rep. Prog. Phys*. **43**, 44 (1980).
29. J.L. García-Palacios and F.J. Lázaro, *Phys. Rev. B* **58**, 14937 (1998).
30. U. Nowak, in: *Annual Reviews of Computational Physics* IX, D. Stauffer (ed.), World Scientific, Singapore, (2000), p. 105.
31. George Marsaglia and Arif Zaman, *Comp. Phys*. **8**, No. 1, 117, (1994).
32. G.M. Wysin, *Phys. Rev. B* **54**, 15156 (1996).
33. B.A. Ivanov, E.G. Galkina, and A.Yu. Galkin, *Fiz. Nizk. Temp*. **36**, 941 (2010) [*Low Temp. Phys*. **36**, 747 (2010)].
34. C.E. Zaspel and G.M. Wysin, *Phys. Rev. B* **90**, 214414, (2014).